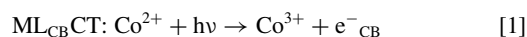| Title	ZnO nanorod-arrays as photo-(electro)chemical materials: strategies designed to overcome the material's natural limitations
Authors	Povey, Ian M.;Kegel, Jan;Pemble, Martyn E.
Publication date	2017-11-30
Original Citation	Kegel, J., Povey, I. M. and Pemble, M. E. (2017) 'ZnO nanorod-arrays as photo-(electro)chemical materials: strategies designed to overcome the material's natural limitations', Journal of the Electrochemical Society, 165(4), pp 3034-3044. doi:10.1149/2.0051804jes
Type of publication	Article (peer-reviewed)
Link to publisher's version	10.1149/2.0051804jes
Rights	© 2017, the Authors. Published by ECS. This is an open access article distributed under the terms of the Creative Commons Attribution 4.0 License (CC BY) which permits unrestricted reuse of the work in any medium, provided the original work is properly cited. All rights reserved. - http://creativecommons.org/licenses/by/4.0/
Download date	2024-04-27 05:04:41
Item downloaded from	https://hdl.handle.net/10468/5236

ZnO Nanorod-Arrays as Photo-(Electro)Chemical Materials: Strategies Designed to Overcome the Material's Natural Limitations

Jan Kegel, [a,z] Ian M. Povey,[a] and Martyn E. Pemble[a,b]

[a]*Tyndall National Institute, University College Cork, Lee Maltings, Cork, Ireland*
[b]*Department of Chemistry, University College Cork, Cork, Ireland*

The urgent need for clean and storable energy drives many currently topical areas of materials research. Among the many materials under investigation zinc oxide is one of the most studied in relation to its use in photo-(electro)chemical applications. This study aims to give an overview of some of the main challenges associated with the use of zinc oxide for these applications: the high density of intrinsic defects which can lead to fast recombination, low visible light absorption and the occurrence of photo-corrosion. Employing simple low-temperature solution based methods; it is shown how defect-engineering can be used to increase the photo-electrochemical performance and how doping can strongly increase the visible light absorption of zinc oxide nanorod-arrays. Furthermore the deposition of ultra-thin titanium dioxide layers using atomic layer deposition is investigated as possible route for the protection of zinc oxide against photo-corrosion.

As one of the most studied metal-oxides Zinc Oxide (ZnO) has already found its way into many industrial applications. Nevertheless enormous research interest is still focused on this earth-abundant, environmentally-friendly material as it offers interesting material properties such as a high exciton binding energy, a direct bandgap and comparably high charge carrier mobility.[1] Furthermore the ability to grow ZnO nanostructures using a wide range of deposition techniques offers new perspectives for the material to be used in opto-electronics.[2] Low-temperature solution based methods are of particular interest as possible routes to the low-cost growth of high surface-area nanostructures for the integration of ZnO into novel energy production and storage devices.[3]

The steadily growing research areas of solar water splitting and photo-catalysis are prominent examples of areas where interest in ZnO-based materials and devices may be found.[4–11] For these applications the nature of the semiconductor/electrolyte interface plays a crucial role. It is of the highest importance to carefully engineer the materials properties in order ensure effective charge carrier transport across the interface. In turn it must be the goal of materials research to tailor the ZnO toward these target applications, where possible addressing the key issues of:

Low visible-light absorption.—Since ZnO exhibits a large bandgap (ca. 3.3 eV) only a small fraction of sunlight is absorbed thus dramatically hindering the use of ZnO for photo-(electro)chemical applications. A common strategy to change the electronic structure of a semiconductor is the introduction of dopants into the host material. In the case of ZnO the material has been doped with various elements whereby many studies focus on doping with transition metals (TMs) such as nickel, magnesium, iron or cobalt.[7,12–17] Historically, research focused on transition metal doping has been fueled by the possible creation of ferromagnetism in these materials – especially in the case of cobalt doping.[12,15,18–21] On the other hand, incorporation of transition metals can also lead to visible light absorption. This is particularly valid for co-doping with cobalt where the presence of the Co^{2+} in the tetrahedral field of the ZnO host lattice leads to sharp d-d transitions[22] as well as charge transfer (CT) between the metal and the ligand conduction band ($ML_{CB}CT$) and between the ligand valance

band and the metal ($L_{VB}MCT$) upon photo-excitation hν:[23,24]

$$ML_{CB}CT: Co^{2+} + h\nu \rightarrow Co^{3+} + e^-_{CB} \quad [1]$$

$$L_{VB}MCT: Co^{2+} + h\nu \rightarrow Co^{1+} + h^+_{VB} \quad [2]$$

The particular electronic structure of ZnO:Co also gives rise to visible light photo-conductivity. It has been shown that the interplay between the d-d transitions and the aforementioned CTs (both closely related to the cobalt concentrations in the films) plays a crucial role for sub-bandgap photoconductivity, which is of high interest for solar energy related research.[23–25] For the synthesis of these materials solution based methods are particularly attractive since they are relatively cheap to employ and operate at low temperatures. However, while different low temperature deposition methods are reported[18,26–29] the direct, low temperature growth of ZnO:Co onto substrates is found to result in comparably low cobalt related d–d visible light absorption.[28,30] A main focus here is therefore the development of simple methods for the growth of ZnO:Co with controllable cobalt concentration and therefore visible light activity.

Fast charge carrier recombination over intrinsic defects.—Intrinsic defects are frequently observed in ZnO grown from various techniques. Depending on their position within the forbidden gap they are characterized as either shallow (possibly ionized) or deep level defects. Generally defects are centers of charge carrier recombination which ultimately limits the efficiency of a photo-electrode. Recombination processes can either occur under radiative conditions (e.g. via the emission of visible light) or non-radiative conditions involving for example thermal relaxation. Radiative recombination processes – which occur on a slower timescale than non-radiative recombination – can be identified using photo-luminescence measurements. For ZnO various light-emitting defect centers (intrinsic but also extrinsic) can be detected using this technique.[2,31,32] The assignment of the photo-luminescence to a specific defect is not always straight forward as the frequently observed, rather broad visible emission for ZnO can have multiple origins contributing to the signal.[32] Furthermore the nature and density of luminescent defects is strongly dependent of the growth technique. Orange emission for example is often observed for ZnO structures grown from solution. The origin of this emission is not yet fully understood and several different explanations

[z]E-mail: jan.kegel@tyndall.ie

have been debated in the literature.[33–38] Since the defect-chemistry will strongly influence the later device performance, careful defect-engineering is necessary to accelerate the use of ZnO as photo-active material.

Photo-corrosion.—As ZnO nanostructures are prone to photo-corrosion it is necessary to develop strategies to protect the material against its self-destruction. Since the photo-corrosion process is dependent on the chemical oxidation potential of the material in respect to the oxidation potential of the electrolyte (e.g. water) a possible route is to adjust the pH value of the electrolyte assuming that the oxidation potential of the material does not change with the same slope as the pH value.[39] Although it has been found that the oxidation potential of ZnO does not shift with the pH of the electrolyte[39] photo-corrosion even occurs in highly alkaline media leading to the decomposition of the material following Equation 3:[40]

$$ZnO + 2h^+ + nH_2O \rightarrow Zn(OH)_n^{(2-n)+} + 1/2 O_2 + nH^+ \qquad [3]$$
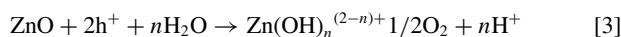
where n depends on the pH value of the electrolyte. The corrosion process itself is thereby believed to include the rapid formation of oxygen molecules under the influence of surface-trapped holes resulting in the expulsion of Zn^{2+}.[41]

Another strategy for the inhibition of photo-corrosion of ZnO is therefore to avoid a direct interface of the material and the electrolyte by employing chemical barrier layers. The barrier itself must again have a suitable oxidation potential in respect to the electrolyte. On the other hand it is also necessary that the layer allows the transport of charge carriers from the underlying material (i.e. suitable energy band alignment with respect to ZnO).[39] A promising example incorporating this strategy is the work on protected Metal-Insulator-Semiconductor structures, which showed stable photo-currents for days or even months.[42–44]

In this study the aforementioned challenges, which hinder the use of ZnO for several photo-electrochemical applications, are addressed. Firstly a route to high visible light absorption by means of the synthesis of cobalt-doped ZnO is reported. Using this method it is possible to control the degree of visible light absorption which is key for the achievement of visible light photo-conductivity in ZnO:Co materials.

Secondly an alternative view on intrinsic defects, which are commonly seen as performance limiting centers of recombination, is presented. Interestingly, intrinsic defects (e.g. oxygen vacancies and zinc interstitials) have been found to aid photo-catalytic reactions.[9,45–47] To take advantage of this curious behavior it is described how intentionally induced defect centers, which give rise to strong orange photo-luminescence, can influence and possibly enhance the photo-electrochemical performance of ZnO.

Finally ZnO-TiO$_2$ core-shell structures were deposited using atomic layer deposition (ALD) – a growth technique known for its good layer uniformity and thickness control. Due to the exceptional chemical stability and theoretically suitable band edge position titanium dioxide (TiO$_2$) may be a suitable chemical barrier layer material for ZnO. These structures were investigated as possible route for the protection of ZnO against photo-corrosion.

Experimental

Seed layer preparation.—The substrates (glass and fluorine-doped tin oxide (FTO) coated glass slides) used in this study were cleaned prior to the seed-layer deposition. Glass substrates were sonicated in a mixture of Millipore water, ammonium hydroxide (NH$_4$OH) and hydrogen peroxide (H$_2$O$_2$) in a ratio of 5:1:1 for 30 min. FTO substrates were sonicated in a solution of decon90 and Millipore water then in acetone and lastly in isopropyl alcohol (IPA) for 30 min each. After the cleaning procedure the substrates were rinsed with Millipore water and blow dried in a stream of nitrogen.

For the preparation of cobalt-doped ZnO nanorod-arrays a Cambridge NanoTech Fiji F200LLC atomic layer deposition (ALD) system was used for the deposition of ZnO seed layers from diethylzinc and water. These films (400 cycles – ca. 70 nm) were grown at a sub-

strate temperature of 190°C and allowed to cool naturally in air. The ALD seed layers were subsequently annealed in air at 300°C for 1 h in a laboratory furnace. It is noteworthy that ALD represents a versatile tool to achieve various nanorod-morphologies simple by adjusting the layer thickness.[48] Also the growth of ZnO nanorod-arrays with higher inter-rod spacing can be achieved using this technique.[49]

The seed layers for one set of orange-luminescent ZnO nanorod-arrays were grown as outlined above. Furthermore, another set of samples was grown on spin-coated seeds (ca. 30 nm thick) whereby the seeding solution was prepared after Greene et al.[50] The different seed-layer deposition methods were employed to investigate whether or not the seed-layer may have an influence on the occurrence of the observed strong orange-luminescence.

For the deposition of ZnO-TiO$_2$ core-shell structures a wet-chemical seeding method was employed following the procedure outlined in Ref. 6.

Solution-based synthesis of ZnO and ZnO:Co nanorod-arrays.—Different chemical routes to the solution-based deposition of ZnO and ZnO:Co nanorod-arrays were used for the three approaches presented here in order to tailor ZnO for photo-(electro)chemical applications. The syntheses outlined were carried out using the following chemicals: zinc acetate dihydrate (ZnAc, reagent grade), zinc nitrate hexahydrate (ZNH, reagent grade), hexamethylenetetramine (HMTA, reagent grade), hydrochloric acid (HCl, 5%wt), 4 M sodium hydroxide solution (NaOH), ethanolamine (EA, reagent grade), cobalt(II) acetate tetrahydrate (CoAc, reagent grade), and Millipore water (H$_2$O).

Synthesis of cobalt-doped ZnO nanorod-arrays.—The growth solution was prepared by adapting a recently reported solution based method.[51] 1.1 g ZnAc and the required amount of CoAc were dissolved in ca. 25 ml H$_2$O under constant stirring for 30 min at room temperature (0.125 g, 0.250 g, 0.374 g for 10%, 20% and 30% Co concentration in respect to Zn concentration in the growth solution, respectively. The term "Co/Zn concentration ratio" is used throughout this article to describe this ratio). Subsequently 7.5 ml of 4 M NaOH solution were quickly added and the solution was allowed to stir for an additional 45 sec after which 5 ml EA was added to the solution. After increasing the volume to 50 ml by adding H$_2$O the growth solution was then left under constant stirring for two hours. The final solution was then transferred to a pre-heated Teflon-lined autoclave. Under a slight angle (ca. 15° of the vertical), the substrates were then immersed into the solution with the seed layer facing down. After closing, the autoclave was put back into a laboratory furnace (115°C). The growth was carried out for 2 h with subsequent natural cooling. Finally the samples were thoroughly rinsed in H$_2$O and blow-dried in nitrogen.

Synthesis of ZnO-TiO$_2$ core-shell structures.—The solution-based deposition of the ZnO nanorod-arrays was carried out as outlined in the previous section but in this case samples were grown in a closed plastic bottle at 85°C for 1 h and without the addition of CoAc. The as-grown ZnO-nanorods were then over-coated with ALD TiO$_2$ using a Cambridge NanoTech Fiji F200LLC system with tetrakis (dimethylamino)titanium (TDMAT) and water as the precursors. First TDMAT was pulsed into the growth chamber (0.3 s) followed by a nitrogen purge (10 s), a H$_2$O pulse (0.1 s) and another nitrogen purge (10 s). This procedure was repeated until a nominal TiO$_2$ thickness of 2 nm, 5 nm or 10 nm was reached (growth rate ca. 0.5 Å/cycle). During the deposition the TDMAT precursor and substrate temperature were held at 90°C and 180°C, respectively.

Synthesis of ZnO nanorod-arrays for defect-engineered photo-electrodes.—Intentionally defect-rich ZnO nanorod-arrays were grown following the solution-based method outlined in Ref. 38. In short, 0.025 M ZNH, 0.15 M HMTA and 4 drops of 5%wt HCl were dissolved in H$_2$O to yield 100 ml of growth solution which was then constantly stirred for 1 h and transferred into a sealable plastic bottle.
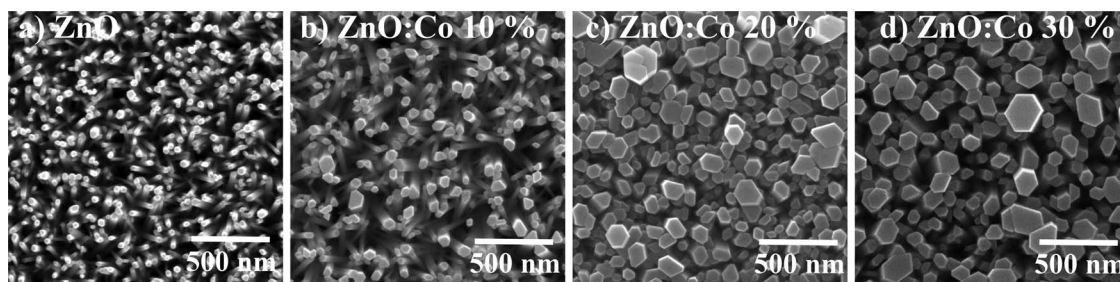
Figure 1. Topview SEM micrographs of undoped (a) and cobalt doped (b-d) ZnO nanorods grown on glass. Percentages given represent the Co/Zn concentration ratio.

Substrates were put in almost vertically with the growth side pointing downwards. The sealed bottle was subsequently put into a standard laboratory oven (95°C, 6 h). After natural cooling of the solution the samples were thoroughly rinsed with H_2O and blow dried with nitrogen.

The as-grown ZnO nanorod-arrays were subjected to post-deposition rapid thermal annealing (RTA) at various temperatures (350°C–550°C) and in various atmospheres (introduced before temperature ramp-up; forming gas (5% H_2 in N_2), Oxygen (O_2) all at 1 bar) using a Jipelec 150 RTA system. The set temperature during RTA was held constant for 10 min.

It is important to note that the different approaches to the solution-based growth of ZnO nanorod-arrays presented above are necessary to achieve the functionality desired in each section. For example, effective cobalt-doping (e.g. intense d-d cobalt-related absorption in the visible range) could not be achieved when the cobalt precursor was simply added to the growth solution used to grow defect-rich ZnO nanorod-arrays (third recipe noted above). On the other hand, the occurrence of strong orange-luminescence post RTA-treatment is only achieved when the nanorod-arrays are grown using this particular recipe. With this in mind, the reader is advised that each sub- results and discussion section is dealt with independently. This is to avoid direct comparison between results of individual sections which may be misleading due to the different synthesis routes used and their possible effect on the material properties.

Materials characterization.—For structural characterization scanning electron microscopy (SEM) and energy dispersive X-ray spectroscopy (EDS) was carried out using a FEI Quanta 650 FEG High Resolution Scanning Electron Microscope equipped with an EDS detector. A Panalytical X'Pert MRD X-Ray diffractometer (Cu Kα radiation λ = 0.1541874 nm, scan resolution 0.02°) in rocking curve configuration was used for X-ray diffraction measurements (XRD). Diffuse reflectance and transmittance spectra in the range of 300–800 nm were recorded by means of a Perkin Elmer 950 UV-Vis spectrometer equipped with an integrating sphere. For the evaluation of the chemical stability the transmission of ZnO-TiO$_2$ core-shell structures under acid exposure (HCl, pH = 2, 15 ml) was constantly measured using an Ocean Optics UV-Vis spectrometer and light source (QE 65000 and HL-2000, respectively). For the recording of transmission electron micrographs (TEM) a JEOL JEM-2100 was used. The photo-electrodes prepared were characterized in a home-made electrochemical cell in 3-electrode configuration (reference electrode = saturated calomel electrode SCE, working electrode = coiled platinum wire). Potential control during cyclic voltammetry (CV), linear sweep voltammetry (LSV) as well as chronoamperometric measurements was achieved using a PalmSens 3 potentiostat. For all photo-electrochemical measurements a solar-simulator (AM 1.5 G, 100 mW/cm^2) was used as a light source. The electrolyte contact area (0.1 M phosphate buffer solution pH = 7) for all investigated photo-electrodes was 1 cm^2. It is important to note that all given current-densities j were not corrected using the actual surface area of the samples but are in respect to the (constant) area of illumination employed (1 cm^2).

Results and Discussion

Cobalt doping for enhanced visible light absorption.—Figure 1 shows SEM micrographs of undoped ZnO (Figure 1a) as well as cobalt doped ZnO:Co with various cobalt concentrations in the growth solution (Figures 1b–1d). Without the addition of cobalt to the growth solution well aligned and thin nanorods are grown. Upon addition of cobalt to the growth solution the rod-diameter increases, resulting in thicker rods (10% Co/Zn concentration ratio in the growth solution) and almost layer like growth with thick crystallites for higher cobalt concentrations (20% and 30% Co/Zn concentration ratio in the growth solution). The growth of ZnO nanorods with lower aspect ratios from solutions with higher Co^{2+} concentration has been observed by other groups as well and has been attributed to a decreasing reaction rate.[28,52–54] In particular the higher solubility products for cobalt-containing species as well as an added reaction barrier due to the conversion of Co^{2+} ions from octahedral to tetrahedral geometries results in a the lower reaction rate.[53,54]

Following the SEM analysis EDS spectra were taken on 3 random spots on each sample (same microscope configurations used for all measurements) in order to calculate an average elemental concentration for each sample. However the exact determination of the oxygen content is difficult using this technique since the detected signals may have larger margins of error. The elemental concentrations given in Table I are therefore only helpful to represent the general trend of the concentrations with varying cobalt concentration in the growth solution.

As a general trend, it can be seen that by increasing the cobalt/zinc ratio the ZnO nanorod-arrays get richer in oxygen. This process does not seem to scale linearly with the Co/Zn concentration ratio and might be influenced by the distinct growth differences between samples with a lower (undoped and 10% Co/Zn concentration ratio in growth solution; nanorod geometry) and higher Co/Zn ratios (20% and 30% Co/Zn concentration ratio in growth solution; densely packed nanorods – almost layer-like). The cobalt concentration of the samples on the other hand does scale with the Co/Zn concentration ratio of the growth solution. The EDS measurements therefore confirm that a higher concentration of cobalt in the growth solution also leads to higher cobalt concentrations in the films and thus possibly also to a higher number of Co^{2+} replacing Zn^{2+} in the ZnO lattice.

Table I. Average elemental concentrations calculated from three random spots on the respective sample. As the detection of oxygen using this method may be subject to some considerable error the table only symbolizes the trend of the elemental concentrations in dependence of the cobalt/zinc concentration ratio in the growth solution.

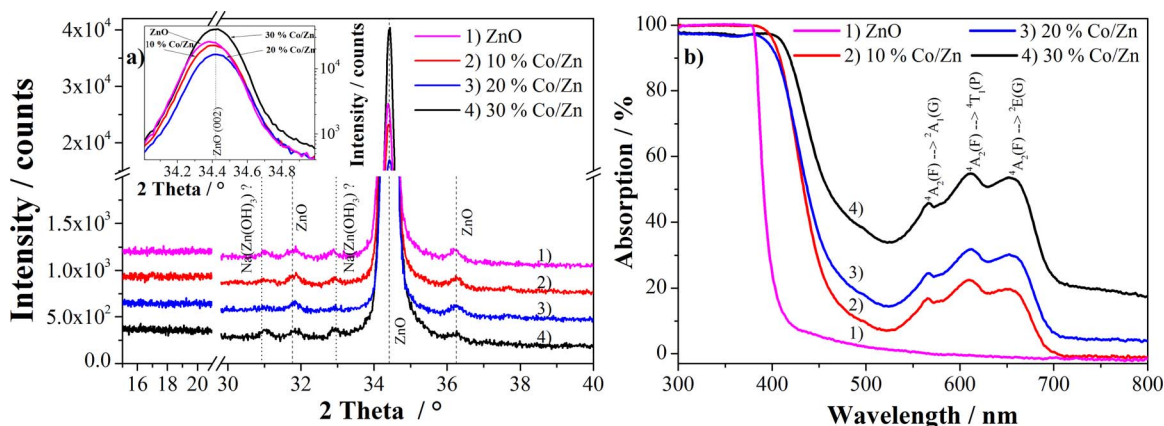| Element	ZnO	ZnO:Co 10%	ZnO:Co 20%	ZnO:Co 30%
O	48.71%	48.81%	53.26%	53.68%
Co	-	0.66%	0.98%	1.33%
Zn	51.29%	50.52%	45.76%	44.99%

Figure 2. a) XRD spectra of undoped and cobalt doped ZnO nanorod-arrays. For better visibility the spectra were offset by 300 counts to each other. Inset: Magnification of the (002) peak revealing a peak shift scaling with the cobalt concentration in the growth solution. b) Absorption spectra of undoped and cobalt doped ZnO nanorod-arrays. The visible light absorption increases with increasing cobalt concentration in the growth solution.

The structural properties of the nanorod-arrays were analyzed by XRD and the results are compiled in Figure 2a. XRD spectra were taken from $2\theta = 15-70°$. As only the ZnO (103) peak (at $2\theta = 62.87°$) was detected in the range for $2\theta > 40°$ Figure 2a focuses on the range $2\theta = 15-40°$. Between $2\theta = 30-40°$ multiple peaks are visible with peak centers being recorded at ca. $31.0°$, $31.84°$, $32.92°$, $34.39°$ and $36.22°$.

The peaks at $31.84°$, $34.39°$ and $36.22°$ are in good agreement with the JCPDS reference card No. 79-2205 – commonly used for the characterization of hydrothermally-grown ZnO[55] – and can be assigned to the ZnO (100), (002) and (101), respectively. Interestingly all samples show additional XRD peaks at $31.0°$ and $32.92°$. As these peaks are found independent of the cobalt concentration in the growth solution (i.e. also the undoped reference samples exhibits these peaks) it is reasonable to expect them to originate from an additional zinc species. Due to the high sodium concentration in the growth solution it is possible that some sort of sodium zincate or sodium zinc hydroxide is formed. For this reason Figure 2a shows the reported peaks of the JCPDS reference card No. 76-0656 for Na(Zn(OH)$_3$), which are close to the observed peaks. However, based on only two XRD peaks a final conclusion about the exact species responsible for the additional peaks at $31.0°$ and $32.92°$ cannot be drawn.

The XRD spectra were also evaluated looking for possible Co containing secondary phases. As many of these cobalt species (e.g. Co(OH)$_2$, Co$_2$O$_3$, CoO and Co$_3$O$_4$) would show an XRD response in the range between $2\theta = 30-40°$ and strong signals between $15-20°$ Figure 2a also evaluates the recorded spectra between $2\theta = 15-20°$. No cobalt related peaks could be detected regardless of the Co concentration in the growth solution.

If cobalt is incorporated in the host lattice one would expect a peak shift in respect to the undoped samples as the doping would result in an increased stress in the material. A shift of the (002) peak to larger angles is indeed what has been observed (inset in Figure 2a) when compared to the undoped sample. As the ionic radius of Co^{2+} (56 pm) is slightly lower than that of Zn^{2+} (60 pm) doping of the nanorods leads to a decrease in the lattice constants and therefore a peak shift toward larger angles.[4] For the prepared cobalt doped samples the peak shift thereby increases with increasing cobalt concentration – an indication of successful doping of the ZnO nanorod-arrays.

UV-Vis spectroscopy measurements were subsequently carried out on the same set of samples. The absorption spectra of the samples are shown in Figure 2b. All cobalt doped samples exhibit a red-shifted absorption edge when compared to the undoped ZnO nanorod-arrays. Additionally strong visible light absorption scaling with the cobalt concentration in the growth solution can be seen for the doped samples. For the sample with a Co/Zn concentration ratio of 30% in the growth solution the absorption in the visible is increased up to 50%$_{abs}$ over

the undoped reference sample. Clear features at ca. 566 nm, 610 nm and 655 nm are noticeable in the absorption spectra of the cobalt doped samples. Earlier studies identify these features as the $^4A_2(F) \rightarrow {}^2A_1(G)$, $^4A_2(F) \rightarrow {}^4T_1(P)$ and $^4A_2(F) \rightarrow {}^2E(G)$ cobalt d-d transitions in the tetrahedral environment of the ZnO lattice[22] indicating the presence of Co^{2+} in a high spin state[15] thus confirming the successful doping of ZnO with cobalt.

It is noteworthy that the method presented here therefore represents an easy route to alternate visible light absorption just by changing the concentrations of the growth precursors in the solution. The control of both visible light absorption and cobalt concentration in the films is an essential factor to consider for the deposition of functional materials such as diluted magnetic semiconductors or materials for photo-(electro)chemical applications. Photo-electrochemical studies of the materials described here are currently underway in our laboratories and will be reported in a separate publication.

Defect-engineered photo-electrodes with enhanced photo-electrochemical performance.—First as-grown ZnO nanorod-arrays grown using the same solution based nanorod growth-technique but using different seed-layer deposition methods were compared with one another to evaluate any differences in their structural, optical end photo-electrochemical properties. Figure 3 shows SEM micrographs, transmission spectra as well as linear sweep voltammetry (LSV) curves of these structures (in the dark and under illumination).

When comparing the alignment and thickness of the nanorods in the SEM micrographs (Figure 3a) it can be seen that nanorods grown on spin-coated seed-layers, using the seeding solution given in Ref. 50, are generally better aligned and thinner. This optical impression of the presence of 'better alignment' was confirmed by XRD measurements (not shown) as the peak associated with the (002) plane of hexagonal ZnO grown on the spin-coated seed layers was far more intense than that for the nanorod-arrays grown on seed-layers deposited by ALD. The reason for the enhanced alignment of the rods on spin-coated seed-layers lies in the preferred (002) orientation of the seed-layer crystallites.[50] The deposited ALD seed-layers do not exhibit a preferred orientation and thus lead to less aligned nanorod-arrays.

Furthermore a direct correlation between the structural and optical properties of the as-grown nanorod-arrays could also be established (transmission spectra in Figure 3). Here it is noticed that nanorods grown on the spin-coated seed layers show an increased transmission over the visible range of the spectrum. The increase in transmission is caused by a reduction of the reflectance of the samples due to the better alignment and possibly thinner rod-diameter. Higher levels of transmission in the visible range are especially important for applications such as dye sensitized solar cells or photo-electrochemical cells using
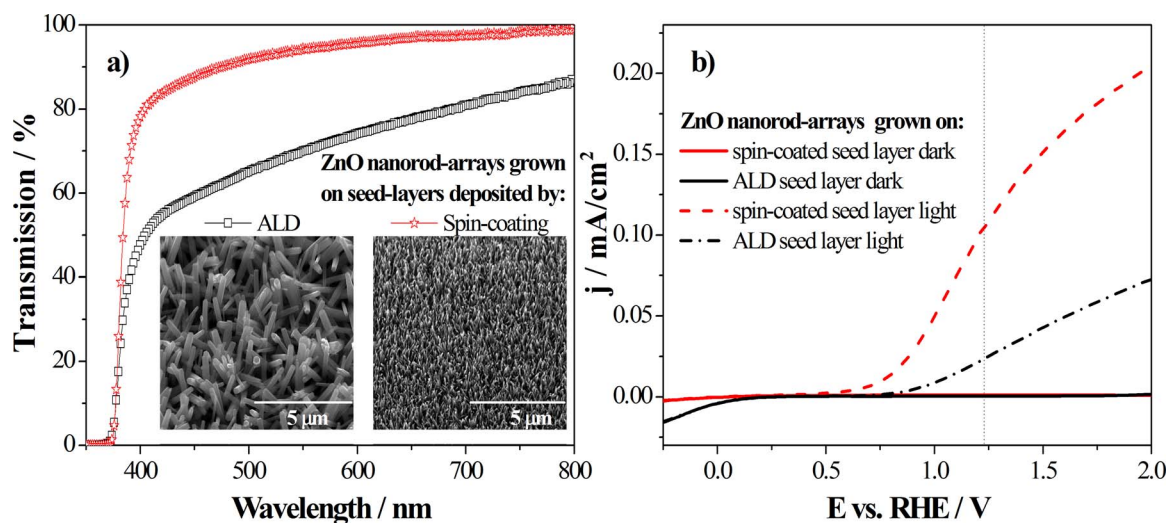
Figure 3. Comparison of as-grown ZnO nanorod-arrays grown on different seed-layers. a) Transmission spectra and SEM micrographs. b) Linear sweep voltammograms of the as-prepared photo-electrodes (illumination: 100 mW/cm^2, AM 1.5 G). Note that the transmission spectra were taken from co-deposited ZnO nanorod-arrays grown on glass.

multiple absorber materials (e.g. a wide-bandgap semiconductor on top of a narrow bandgap material).

Figure 3b shows the LSV curves of as-grown ZnO nanorods grown on different seed layers. Both samples show comparable dark currents with only a small current being detected in the reductive part of the curve. No significant oxidative current can be noticed for the samples. However, under illumination with simulated sunlight (AM 1.5 G, 100 mW/cm^2) both electrodes show a considerable oxidative photo-current. Here the onset potential of the photo-current is shifted toward more negative potentials for the sample grown on the spin-coated seed layer (ca. 0.5 V compared to 0.75 V for nanorod-arrays grown on the ALD seed layer). Also the magnitude of the photo-current is essentially higher for the sample grown on spin-coated seed layers. At 1.23 eV vs. RHE this photo-electrode generates ca. 0.1 mA/cm^2 compared to 0.023 mA/cm^2 observed for ZnO nanorods grown on seed layers deposited by ALD.

As the current densities given in the figure are in respect to the illuminated area it seems appropriate to attribute the better performance of the ZnO nanorod-arrays grown on the spin-coated seed layers to the bigger surface area due to the thinner diameter of the rods. However, it can also be seen that the slope with which the photo-current rises is steeper than for the nanorods grown on ALD seeds and no saturation is reached at higher positive potentials. For this reason these features cannot solely be related to the surface area of the samples. It is proposed that they are actually indicative of a lower rate of recombination (steeper rise of photo- current) as well as a greater number of photo-generated holes participating in chemical reactions with the electrolyte (saturation of photo-current). For the nanorod-arrays grown on spin-coated seed layers the lower recombination rate could result from the thinner rod diameter as it easier for bulk charge carriers to reach the interface where they can be separated. Additionally it is reasonable to expect a higher saturation current from these samples as the reflection is lower compared to the nanorod-arrays grown on seed layers deposited by ALD.

Subsequently rapid thermal annealing was used to alter the defect composition of the as-grown ZnO nanorod-arrays. Samples grown on ALD seed layers were annealed in forming gas (5% H$_2$ in N$_2$; 350°C, 430°C, 550°C) and the nanorod-arrays grown on spin-coated seed layers were exposed to oxygen during RTA (350°C, 450°C, 550°C). Additionally, ZnO nanorod-arrays grown on different substrates and seed layers were subjected to RTA in oxygen at 450°C to evaluate the influence that different substrates or seed layers might have on the defect composition.

Figure 4 compiles the PL spectra of the annealed samples as well as the LSVs recorded from the photo-electrodes. Focusing on the photo-luminescence results first (Figures 4a and 4b), all samples investigated show a more or less sharp response in the near UV region and a broad emission in the visible range. For the as-grown samples in Figures 4a and 4b the center of the near UV peak is located at 390 nm and the visible emission is centered at around 575 nm (yellow). The broad feature in the visible is frequently observed for samples grown from solution and the origin of this emission has mainly been attributed to surface adsorbents from the growth solution.[33,34,38] As the band-band recombination of ZnO would be expected to be closer to 380 nm the peak in the near UV is likely caused by contributions of multiple recombination processes (i.e. band-band and recombination over shallow defects). A shift of the near UV peak towards 380 nm can be seen for samples annealed at 350°C, indicating increased direct recombination between the energy bands due to improved crystallinity of the rods and passivation of non-radiative defects. The latter is especially valid when forming gas is used as the annealing atmosphere since hydrogen is known to passivate non-radiative defects – especially those at the surface.[33,34] Furthermore the yellow emission is decreased due to desorption of surface adsorbents at elevated temperatures.[56]

When the annealing temperature is increased (430°C for forming gas) and (450°C for O$_2$) the near UV peak decreases again but strong orange emission (centered around 600 nm) is noticed for both samples making recombination induced by this defect center the dominant recombination channel. The appearance of the orange-emission is seen to be highly temperature dependent but atmosphere independent (i.e. reductive as well as oxidative atmospheres lead to orange-emission). Furthermore it has recently been shown that strong-orange emission occurs for various annealing atmospheres at ca. 450°C while keeping the seed-layer deposition the same.[38]

It is noteworthy that samples prepared on ALD deposited seed layers showed generally less orange emission when compared to nanorod-arrays grown on spin-coated seed layers. When co-annealing nanorod-arrays prepared on different seed layers and different substrates (glass, gallium nitride, FTO, sapphire) it was found that the substrate does not influence the orange emission. However, for the combination FTO + ALD seed layer the orange emission was found to be the lowest among all samples. Furthermore, this substrate-seed layer combination also showed the worst alignment and coverage, which may point towards an influence of the structural properties on the photo-luminescence. It is however important to point out that orange-emission for nanorod-arrays annealed at temperatures of ca. 450°C occurs
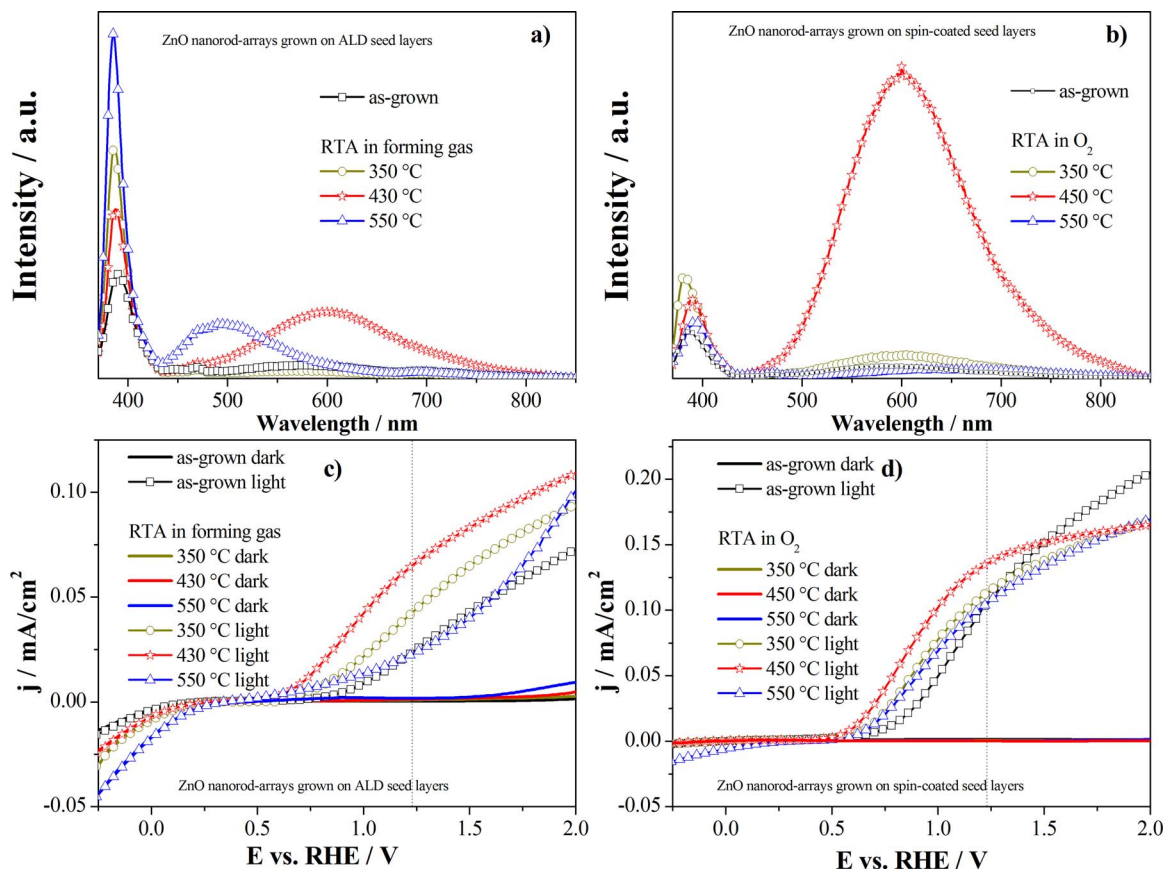
Figure 4. Photo-luminescence spectra and corresponding linear sweep voltammograms of RTA treated ZnO photo-electrodes; a) and c) for samples grown on ALD deposited seed-layers (RTA in forming gas). b) and d) for samples grown on spin-coated seed-layers (RTA in O$_2$). Illumination: 100 mW/cm^2, AM 1.5 G. Electrolyte: 0.1 M phosphate buffer solution (pH = 7).

regardless of the seed-layer used. This in turn rules out that the seed-layer is responsible for the observed PL characteristics.

For a detailed discussion on the observed orange emission and its nature the reader is referred to recent literature.[38] In that paper evidences have been presented that the oxygen vacancy-zinc interstitial defect complex V$_O$-Zn$_i$ might be responsible for the observed orange emission. Due to advances in computational studies of ZnO over the past decades, it is now widely accepted that the deep-level oxygen vacancy is thermodynamically stable in its neutral V$_O$ and doubly ionized state V$_O^{++}$ with V$_O$ being more abundant due to the lower formation energy.[2,32] The singly ionized oxygen vacancy V$_O^+$ is thermodynamically unstable but can be created e.g. by light illumination.[57,58] A zinc interstitial defect on the other hand resides shallow close to the conduction band and can thus be ionized at room temperature (Zn$_i^{++}$ is the stable state).[36,59] The formation of the V$_O$-Zn$_i$ defect-complex may seem counter-intuitive at first given the donor-like nature of both intrinsic defects. However, it has been demonstrated that the defect-complex might exist upon kinetic formation via a kick-out process.[60] Kim et al. found the quantum mechanical hybridization between the electronic orbitals of the deep- and shallow-donor states (V$_O$, and Zn$_i$, respectively) responsible for the strong attraction between the individual defects.[61] A related, interesting aspect is that highly oxygen deficient materials were calculated to have a higher concentration of zinc interstitials when an interaction of these two defects is allowed. This would lead to the creation of more ionized zinc interstitials and in turn enhanced n-type character.[61] Furthermore it is worth noting that the number of possible charge transition states is increased the closer the two point defects are together. This can lead to changes in the opto-electronic properties (e.g. intrinsic n-type doping and photo-luminescence) as compared to the single point defect case.[60,61] In the opinion of the authors it would therefore be interesting to investigate

whether it is possible for the V$_O$-Zn$_i$ complex to stabilize an oxygen vacancy in its singly ionized state which, due to its spin dependent recombination processes,[62] could help to identify the exact recombination mechanism for the observed orange emission.

Interestingly the orange emission disappears when the ZnO nanorod-arrays are annealed at higher temperatures (550°C) – again, irrespective of the annealing atmosphere. However, these higher annealing temperatures lead to the introduction of additional defects, which is especially visible for the sample annealed in forming gas. Here a strong emission centered around 490 nm is detected which might be the result of some destructive, decomposition processes at the surface of the nanorods.[2] Indeed strong material damage for samples annealed at 600°C was observed optically.

When correlating the observed PL properties to the photo-electrochemical performance of those samples (LSV voltammograms in Figures 4c and 4d) it can be seen that annealing of the samples leads to a cathodic shift of the photo-current onset potential when compared to the as-grown reference samples. Interestingly the samples exhibiting strong orange-luminescence show the biggest shift as well as a steeper rise of the photo-current leading to significantly improved photo-current densities at 1.23 V vs. RHE (dotted line in the figures). These *j-V* characteristics are especially important for real working devices as a main goal of solar water splitting is to achieve the highest possible photo-current under the lowest possible applied bias potential.

The cathodic shift of the photo-current onset potential is the result of an improved hole transfer rate of the electrodes.[63] Both the charge carrier concentration (here donor type) as well as charge carrier recombination have big influence on the photo-current onset potential as well as the photo-current density in general.[64] Assuming that the Fermi energy is not "pinned" to the surface, a high charge carrier density
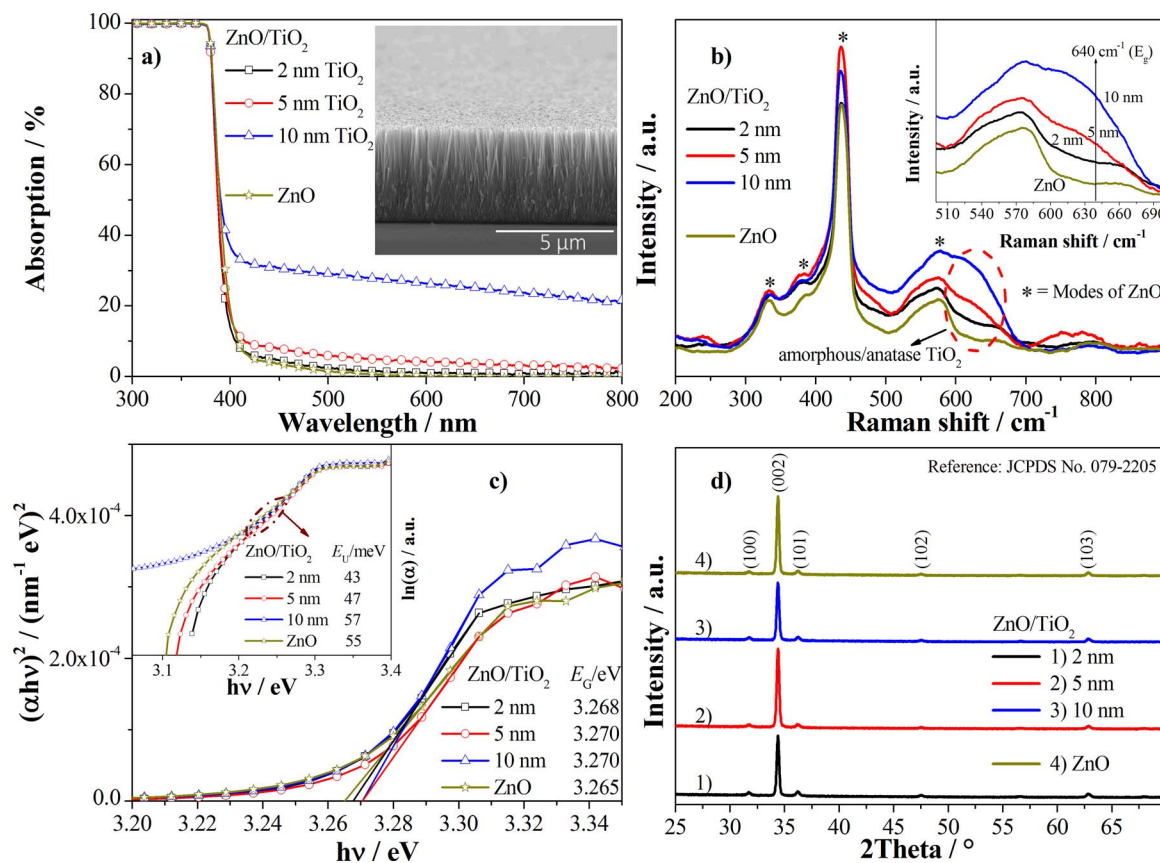
Figure 5. Material properties of ZnO-TiO$_2$ core-shell nanorod-arrays with varying TiO$_2$ layer thickness (2 nm, 5 nm, 10 nm): a) optical absorption spectra. Inset: SEM micrograph (ZnO), c) Tauc-plot for the estimation of the bandgap energies E_G. Inset: estimation of the Urabach energy E_U, b) Raman spectra, d) XRD spectra.

increases the band bending at the semiconductor-electrolyte interface and thus also the driving force for holes to oxidize the electrolyte.

Charge carrier recombination on the other hand affects the photo-current i_{ph} directly and its effects are also visible in the slope of the j-V curve of a photo-electrode. An immediate and steep increase of the photo-current is an indication of a lower or slower rate of recombination in the bulk, the space charge region as well as the surface of a photo-electrode. This is indeed what is observed for samples with strong orange luminescence. Considering the possible slow trapping of a photo-generated electron by the orange-luminescent defect the recombination with a photo-generated hole in the valence band might be delayed. This would in turn result in an increased probability for the hole to diffuse to the space charge region (generation in the bulk) or toward the surface (generation in the space charge region). Furthermore trapped electrons might contribute to the enhanced photo-current density as well.

Nonetheless, for the sample annealed in O$_2$ at 450°C (very strong orange emission) the photo-current seems to plateau at a lower value when a higher positive bias potential is applied (Figure 4d). To what extent the orange-luminescent defects are responsible for the current saturation has to be established in further investigations. However, when assuming that the V_O-Zn_i defect complex is responsible for the observed orange emission it is possible that plateau of the photocurrent is the result of an increased charge carrier concentration, which has been shown to reduce the saturation current.[64]

ZnO-TiO$_2$ core-shell structures with improved photo-electrochemical stability.—In order to evaluate the chemical stability and the photo-corrosion behavior of the TiO$_2$ over-coated ZnO nanorod-arrays different layer thicknesses of the TiO$_2$ barrier

layer were deposited. The as-deposited core-shell structures were characterized in order to get some insight in the optical and structural material properties. Figure 5 summarizes the material properties of the as-grown TiO$_2$-ZnO core-shell nanorod-arrays.

Upon over-coating the ZnO nanorods with thicker TiO$_2$ layers (5 nm and 10 nm) an optical color change (samples appear brownish) can be noticed. These impressions have been verified by UV-Vis spectroscopy in Figure 5a. A thin TiO$_2$ layer (2 nm) does not show a significant difference in the absorption spectra when compared to the ZnO reference sample. However, for thicker layers – especially for the sample with 10 nm TiO$_2$ over-coating – a significant increase in visible light absorption can be noticed. The brownish color and the higher visible light absorption point towards possible carbon contamination of these samples. As the samples where pre-cleaned in oxygen plasma prior to the ALD deposition it appears likely that the contamination is a direct result of the ALD deposition (e.g. residue of the titanium precursor).

To prove whether the high visible-light absorption is caused by a change of the underlying ZnO a Tauc analysis[65] of the absorption data has been carried out (Figure 5b). This analysis allows the estimation of the bandgap energy E_G. For the uncoated ZnO reference the so-determined E_G is 3.265 eV. The TiO$_2$ coated samples show bandgap energies of 3.268 eV and 3.270 eV for 2 nm and 5 nm/10 nm layer thickness, respectively.

For the ZnO-TiO$_2$ core-shell structures no definitive dependence of the bandgap energy on TiO$_2$ layer thickness is apparent. Indeed the estimated bandgap energies of all samples – including the ZnO reference – are very similar to each other giving rise to the conclusion that the electronic structure of the underlying ZnO has not been affected by TiO$_2$ deposition and that the increased visible-light absorption is most likely related to contamination.
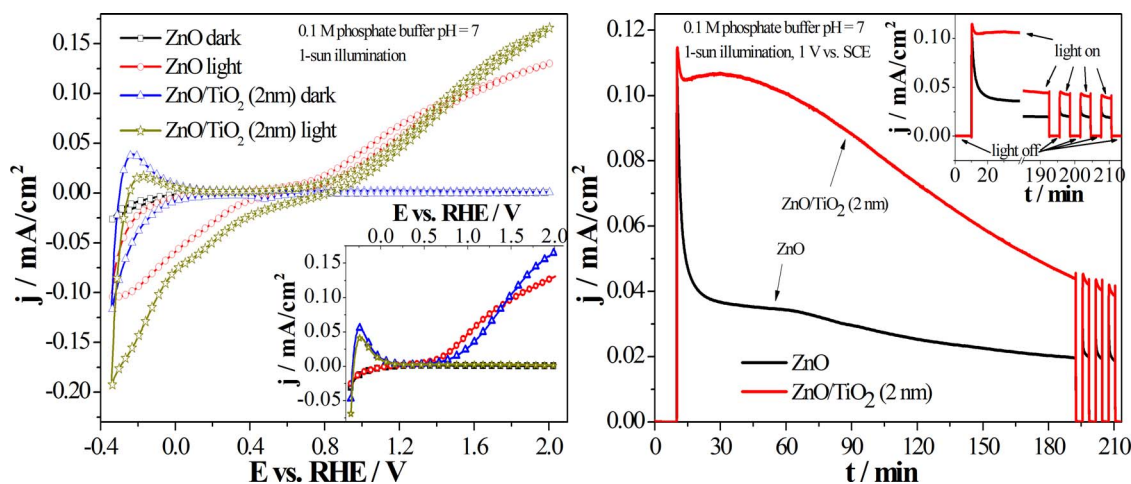
Figure 6. Left: Voltammograms (-1 V – 1.35 V vs. SCE, scan rate 50 mV/s) of uncoated ZnO and ZnO-TiO$_2$ (2 nm) core-shell nanorod-arrays grown on FTO in the dark and under illumination (1-sun). Inset: linear sweep voltammetry (LSV) spectra for the investigated samples (electrodes were hold at -1 V vs. SCE for 5 seconds before the sweeping to positive potentials). Right: Chronoamperometry measurements on the same samples at 1 V vs. SCE (1.66 V vs. RHE). 0.1 M phosphate buffer solution (pH = 7) has been the electrolyte for both measurements. Illumination: 100 mW/cm^2, AM 1.5 G.

From the UV-Vis measurements the Urbach energies E_U for all samples were also estimated. The inset in Figure 5c shows the analysis of the logarithm of the absorption coefficients for the estimation of E_U (here the slopes of the linear part for photon energies h$\nu < E_G$ were taken for the determination). Interestingly the Urbach energy was found to increase for thicker TiO$_2$. When compared to the uncoated ZnO sample an over-layer of 2 or 5 nm TiO$_2$ E_U even decreased and a 10 nm thick layer reaches a comparable value in respect to the reference sample.

As the Urbach energy is commonly taken as a measure of structural disorder or energetic states near the band-edges (band-tail states) of a semiconductor a low Urbach energy corresponds to a material with low density of energetic states (e.g. structural or surface defects) localized near the band-edges. For the TiO$_2$ coated samples it is thus obvious that the deposition of the protective layer did not lead to an increased density of these states. The reduction of same implies that the electronic properties of the coated samples (2 nm and 5 nm) may even have been improved.

As the 10 nm thick TiO$_2$ layer did not show an improvement of the Urbach energy compared to the uncoated sample, the heat-treatment that occurred during the ALD process (180°C; i.e. annealing) cannot be responsible for the observed behavior. It is more likely that for thinner layers surface defects are passivated similarly to the findings of Liu et al.[66]

In order to gain some insight in the structural properties of the core-shell structures Raman and XRD measurements were carried out and are summarized in Figures 5b and 5d, respectively. The XRD measurements of the samples showed only ZnO related peaks with the response from the (002) plane as the most pronounced, confirming the good alignment of the grown ZnO nanorods – also visible in the SEM micrograph in Figure 5a. No TiO$_2$ related signals have been detected. Also the Raman spectra show mostly ZnO related peaks but significant differences can be seen between 600 cm^{-1} and 650 cm^{-1}. A more intense signal in this region was observed with increasing TiO$_2$ layer thickness. The inset in Figure 5b magnifies this range. It can be seen that especially for the 5 nm and 10 nm thick TiO$_2$ layers the features near 640 cm^{-1} become more prominent. It is noteworthy that the E$_G$ mode of anatase TiO$_2$ occurs in this spectral region.[67] Since the feature is very broad and a clear peak is absent, the as-deposited TiO$_2$ possesses only a limited degree of long-range order as compared to the anatase phase.[67] Thus it appears likely that the TiO$_2$ films are an amorphous-anatase mixed phase.

Following the initial material characterization of the ZnO-TiO$_2$ core-shell structures the photo-electrochemical performance of samples grown on FTO was evaluated. As an example cyclic voltammetry

(CV), LSV (both left panel) and chronoamperometry (CA, right panel) measurements for the unprotected and the core-shell samples with a TiO$_2$ layer thickness of 2 nm are shown in Figure 6.

In the dark both samples do not show a significant current for water oxidation. Interestingly the TiO$_2$ coated sample shows a higher reductive dark current as well as a sharp oxidative peak at –0.2 V vs. RHE (CV scans, left panel of Figure 6). Since the CV measurements were recorded starting at 0 V vs. SCE scanning toward positive potentials (up to 1.35 V vs. SCE) and then sweeping back toward the negative end (-1 V vs. SCE), the observed behavior might result from a charging of the TiO$_2$ or the TiO$_2$/ZnO interface and subsequent rapid discharging in the potential range from -1 V -0.640 V vs. SCE (-0.343 V – 0.017 V vs. RHE). In support of a possible charging/discharging effect – which would resemble the reduction/oxidation of TiO$_2$ – is the observation of the so called proton insertion Reaction 4 by other groups:[68–70]

$$Ti^{IV}O_2 + e^- + H^+ \rightarrow Ti^{III}OOH \qquad [4]$$
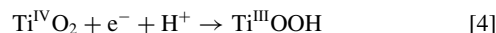
A sufficiently high reductive potential leads thereby to the formation of Ti^{III} donor centers of which the charge is compensated by the proton. This reaction is frequently utilized as route for the doping of TiO$_2$. Interestingly it has been reported that this reaction manifests itself more strongly in acidic media.[70] If the observed CV behavior of the electrodes presented here is associated with the proton insertion reaction this might point toward a local pH difference at the electrode surface.

Under simulated sunlight both samples show an increase of the reductive current at low potentials vs. RHE as well as an oxidative photo-current toward more positive potentials as compared the non-illuminated case. The unprotected sample shows an earlier photo-current onset potential compared to the ZnO-TiO$_2$ core-shell structure. However, when more positive potentials are applied, the samples perform comparably with the protected, TiO$_2$ coated sample exhibiting an even steeper rise of the photo-current. It is also necessary to make the reader aware of the fact, discussed in a previous publication, that while measuring multiple ZnO-TiO$_2$ samples very early photo-current saturation has been observed for some samples.[71] However, after evaluating the data collected from multiple samples the core-shell structure presented here seems more representative.

The observed increase of the reductive current upon illumination is in fact the manifestation of back-reactions on the electrode surface. Since the oxidation of water involves multiple steps and intermediate products[72] illumination and subsequent rapid scanning toward positive potentials leaves oxidation intermediates in close proximity to the electrode surface. This is particularly true for the cell configuration
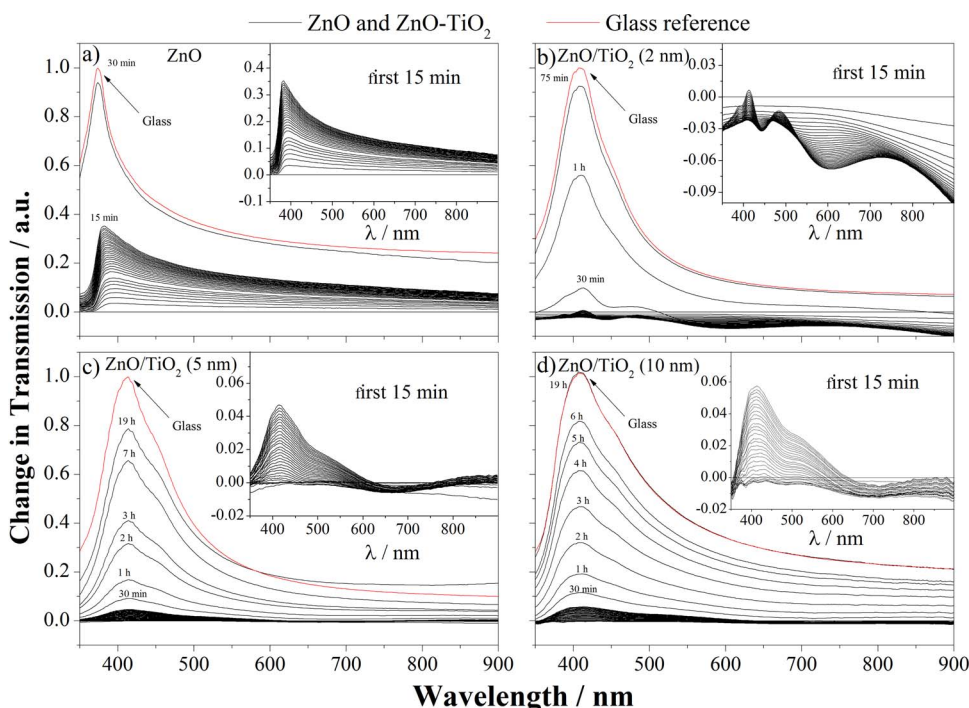
Figure 7. Change of optical transmission over time for samples being exposed to hydrochloric acid (pH = 2) – a) ZnO b) ZnO-TiO$_2$ with 2 nm TiO$_2$ c) ZnO-TiO$_2$ with 5 nm TiO$_2$ d) ZnO-TiO$_2$ with 10 nm TiO$_2$. A positive change in transmission represents possible dissolution of ZnO. Please note that the shape of the spectra (especially < 400 nm) cannot be correlated to electronic properties of the samples (e.g. bandgap absorption) as the light source used is not intended for measurements in the UV range.

used in this study, where the electrode is in a horizontal position and the electrolyte is not agitated. An increased current when scanning to negative potentials is thus due to the back-reaction of these intermediates. Further proof of this behavior can be found in the LSV scans of the samples (inset in the left panel of Figure 6). Here – when scanning from negative to positive potentials – no change of the reductive current is observed and the traces of the dark and light measurements on the respective samples are essentially the same for the reductive part of the spectrum. The earlier photo-current onset potential for the uncoated sample is also visible in the LSVs. This is an indication of a better initial catalytic charge transfer rate at the electrode surface for the plain ZnO sample. However, when the potential is increased and the catalytic hurdle for water oxidation is decreased charge carrier recombination becomes a major rate limiting factor. Here the photo-current for the ZnO sample increases steeply at the beginning but flattens towards higher potentials. In particular the flattening of the photo-current is not as dramatic for the ZnO-TiO$_2$ core-shell structure in the potential range examined. Thus it might well be that charge carrier recombination is reduced for the core-shell structure, similarly to the results of an earlier study.[66]

When biased at 1 V vs. SCE (1.66 V vs. RHE) for a longer period of time (CA measurements in right panel in Figure 6) a stabilization of the photo-current can be observed for the ZnO-TiO$_2$ core-shell structure. The strong drop in the photo-current observed for the ZnO reference sample is not visible for this sample. The core-shell sample even shows an initial increase in photo-current (from ca. 5 min after the light is turned on) which then levels at ca. 0.107 mA/cm^{-2}. However, after 1 h the photo-current also decreases significantly for the protected sample.

The ultra-thin TiO$_2$ over-coating presented here is able to chemically protect the underlying ZnO as evidenced by the CA measurements. When evaluated over the entire measurement period of 3 h the ZnO-TiO$_2$ core-shell structure generates more current than the ZnO reference. However, the initial increase in photo-current and the strong decrease of the current after ca. 1 h indicate that photo-corrosion processes still occur. These observations can be explained by arguing that

the TiO$_2$ over-coating is not pinhole free leaving a small area of ZnO unprotected. Over the course of the measurement the exposed ZnO area gets bigger since the photo-corrosion process leads to removal of material in those areas where the TiO$_2$ layer exhibits pinholes. The removal of material may lead to the complete collapse of the TiO$_2$ protection layer. Due to the exposure of a greater area of ZnO to the electrolyte the photo-current initially increases. After prolonged measurement the photo-corrosion process therefore increases, resulting in the observed decrease in photo-current. Similar behavior could be observed for samples coated with thicker TiO$_2$ layers. These samples were able to protect the underlying ZnO for a longer time but the initial photo-current of these samples were found significantly reduced.

In order to evaluate the proposal that the protective layers were not entirely pin-hole free ZnO-TiO$_2$ core-shell structures with varying TiO$_2$ thickness grown on glass were exposed to hydrochloric acid (pH = 2) and the optical transmission properties measured over time during this process. For these measurements the transmission of the samples in contact with water were taken as the baseline and the change in transmission was then recorded over time once the samples were put in contact with the acid. Finally the transmission spectra recorded in this manner were weighted to the normalized spectrum of a plane glass slide in contact with the acid. The spectrum of the glass slide was taken after each long-term measurement on the respective sample. A loss of material due to possible chemical dissolution of ZnO should therefore be visible by a positive change of transmission.

Figure 7 summarizes the optical measurements for the ZnO reference sample as well as for ZnO-TiO$_2$ structures with 2 nm, 5 nm and 10 nm TiO$_2$ layer thickness. The change in transmission for the unprotected sample is close to that of the glass slide after about 30 min. A significant delay of the change in transmission towards that of the glass slide is visible for all TiO$_2$ coated samples. For the 2 nm sample the transmission is close to the transmission of glass after ca. 75 min. However, for the samples with the thicker coatings, 5 nm and 10 nm, only slight differences are visible and the transmission for these samples approaches that of the glass slide after ca. 19 h.
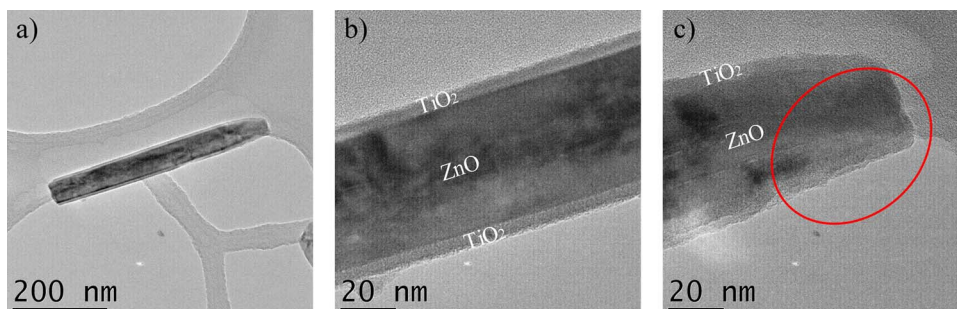
Figure 8. TEM images of a ZnO nanorod over-coated with 5 nm TiO_2 a) overview b) and c) magnification of the rod side-facets and the rod tip, respectively. The TiO_2 growth is non-conformal on the rod-tip.

From the measurements of the change of transmission upon acid exposure it can be seen that protective layers consisting of 5 nm and 10 nm of TiO_2 protect the underlying ZnO well from the acid for a prolonged period of time. However some dissolution also occurs for these samples. During the measurements it was observed optically that the nanorod-arrays were partly flaking off – especially for the 10 nm TiO_2 sample. Thus suggesting that the acid might be mainly attacking the bottom of the structures, leading to etching of the seed-layer. The 2 nm TiO_2 sample on the other hand did not exhibit flaking at the seed layer substrate interface. Nevertheless the rapid dissolution of this core-shell structure verifies the proposal that a 2 nm thick TiO_2 layer most likely contains a larger number of pinholes. Interestingly this sample showed an initial negative change in transmission – especially during the first 15 min of the experiment. The recorded transmission curves for this period are shown in the inset of Figure 7b and differ significantly in their magnitude when compared to all other samples (insets in Figures 7a, 7c and 7d). When the photo-corrosion process described for this TiO_2 layer thickness (refer to Figure 6 and related comments) is taken as an explanation for the observed chemical dissolution in the acid exposure experiment, it is possible that the partial etching of the ZnO material in the pin-hole rich areas could lead to a micro-roughening of the surface of the core-shell structures. In turn this might lead to an increased reflection in the visible range of the spectrum resulting in a decrease in transmission.

Indeed pin-hole rich TiO_2 layers could be observed in TEM measurements as the example-images for the 5 nm TiO_2 sample in Figure 8 show. The overview in Figure 8a shows that the TiO_2 layer along the edges of the rod is homogenous and the nominal layer thickness of 5 nm was achieved (Figure 8b). However, a closer view of the rod tips reveals an incomplete TiO_2 layer in this area (Figure 8c). As this phenomena has been observed on multiple rods (especially for the 2 nm TiO_2 sample) it seems likely that TiO_2 nucleation and growth on the tip of the rod is somewhat inhibited. In particular a nucleation delay on the crystal facets of the tips seems likely. The non-conformal TiO_2 growth is thus making photo-corrosion as well as chemical dissolution of the underlying ZnO possible. Thus, future research will focus on improving the rod-tip coverage, possibly by optimizing the TiO_2 ALD.

fect of different seed layer deposition techniques has been compared and the results suggest a large influence on the material properties of the ZnO nanorod-arrays grown subsequently.

A doping strategy has been presented which can be applied in order to shift the materials absorption into the visible region. As the large bandgap energy of ZnO, some 3.3 eV ($<$ 380 nm), limits the absorption of sunlight significantly, it is demonstrated that visible light absorption can be achieved by the incorporation of significant amounts of cobalt into the ZnO host lattice using a newly developed low-temperature solution-based growth method. It is shown that the visible-light absorption of the resulting material, which consists of ZnO:Co nanorod-arrays directly deposited onto seed-layer coated glass substrates, extends up to 700 nm by controlling the cobalt concentration in the growth solution.

Lastly, the issue of photo-corrosion of ZnO-based photo-electrodes was addressed. In order to produce effective and stable chemical barriers pin-hole free layers are essential. This requirement was approached using atomic layer deposition (ALD) which offers the advantage of controlled and nominally pin-hole free deposition of ultrathin barrier layers even onto 3D-geometries. It has been shown that TiO_2 shells are able to chemically protect the ZnO core in acidic media. However, it was found that for some samples the TiO_2 barriers are not complete – especially at the rod tips – leading to a considerably lower etch rate as compared to uncoated nanorod-arrays. Photo-electrochemically core-shell structures with 2 nm TiO_2 coating showed a photo-current stabilization for several hours with a net gain in generated current over time.

ORCID

Jan Kegel https://orcid.org/0000-0003-1729-4503

Conclusions

Strategies for the minimization of the undesirable influences associated with the high rate of fast charge carrier recombination, low visible light absorption and photo-corrosion for ZnO nanorod-arrays grown from solution have been introduced.

It is demonstrated that careful defect-engineering may be used to increase the efficiency of photo-(electro)chemical reactions. Here, the specific focus was directed toward orange-luminescent defect-centers. Linear sweep voltammetry in neutral electrolyte solution revealed that ZnO nanorod-arrays exhibiting strong orange emission show a defect-promoted increase in photo-current under simulated sunlight of about 200% as compared to as-grown nanorod-arrays. Additionally, the ef-

References

1. H. Morkoç and Ü. Özgür, in *Zinc Oxide–Fundamentals, Materials and Device Technology*, p. 131, Wiley-VCH Verlag GmbH & Co. KGaA (2009).
2. A. B. Djurišić, A. M. C. Ng, and X. Y. Chen, *Progress in Quantum Electronics*, **34**, 191 (2010).
3. S. Xu and Z. L. Wang, *Nano Research*, **4**, 1013 (2011).
4. Y. Lu, Y. Lin, D. Wang, L. Wang, T. Xie, and T. Jiang, *Nano Research*, **4**, 1144 (2011).
5. Y. Mao, H. Yang, J. Chen, J. Chen, Y. Tong, and X. Wang, *Nano Energy*, **6**, 10 (2014).
6. L. Cai, F. Ren, M. Wang, G. Cai, Y. Chen, Y. Liu, S. Shen, and L. Guo, *International Journal of Hydrogen Energy*, **40**, 1394 (2015).
7. W. C. Lee, G. E. Canciani, B. O. S. Alwhshe, and Q. Chen, *International Journal of Hydrogen Energy*, **41**, 123 (2015).
8. J. Kaur, S. Bansal, and S. Singhal, *Physica B: Condensed Matter*, **416**, 33 (2013).

9. J. Wang, Z. Wang, B. Huang, Y. Ma, Y. Liu, X. Qin, X. Zhang, and Y. Dai, *ACS applied materials & interfaces*, **4**, 4024 (2012).
10. K. S. Ranjith, R. Pandian, E. McGlynn, and R. T. Rajendra Kumar, *Crystal Growth & Design*, **14**, 2873 (2014).
11. F. Kayaci, S. Vempati, C. Ozgit-Akgun, N. Biyikli, and T. Uyar, *Applied Catalysis B: Environmental*, **156–157**, 173 (2014).
12. S. B. Ogale, *Advanced materials*, **22**, 3125 (2010).
13. S. V. Bhat and F. L. Deepak, *Solid State Communications*, **135**, 345 (2005).
14. S. Basu, D. Y. Inamdar, S. Mahamuni, A. Chakrabarti, C. Kamal, G. R. Kumar, S. N. Jha, and D. Bhattacharyya, *The Journal of Physical Chemistry C*, **118**, 9154 (2014).
15. D. Y. Inamdar, A. D. Lad, A. K. Pathak, I. Dubenko, N. Ali, and S. Mahamuni, *The Journal of Physical Chemistry C*, **114**, 1451 (2010).
16. V. Sharma, M. Dixit, V. R. Satsangi, S. Dass, S. Pal, and R. Shrivastav, *International Journal of Hydrogen Energy*, **39**, 3637 (2014).
17. S. Benramache, B. Benhaoua, and H. Bentrah, *Journal of Nanostructure in Chemistry*, **3**, 54 (2013).
18. R. Elilarassi and G. Chandrasekaran, *Journal of Materials Science: Materials in Electronics*, **24**, 96 (2012).
19. V. Gandhi, R. Ganesan, H. H. Abdulrahman Syedahamed, and M. Thaiyan, *The Journal of Physical Chemistry C*, **118**, 9715 (2014).
20. H.-J. Lee, S.-Y. Jeong, C. R. Cho, and C. H. Park, *Applied Physics Letters*, **81**, 4020 (2002).
21. I. Djerdj, Z. Jaglicic, D. Arcon, and M. Niederberger, *Nanoscale*, **2**, 1096 (2010).
22. P. Koidl, *Physical Review B*, **15**, 2493 (1977).
23. C. A. Johnson, T. C. Kaspar, S. A. Chambers, G. M. Salley, and D. R. Gamelin, *Physical Review B*, **81**, 125206 (2010).
24. J. W. May, J. Ma, E. Badaeva, and X. Li, *The Journal of Physical Chemistry C*, **118**, 13152 (2014).
25. C. A. Johnson, A. Cohn, T. Kaspar, S. A. Chambers, G. M. Salley, and D. R. Gamelin, *Physical Review B*, **84**, 125203 (2011).
26. P. M. Aneesh, C. T. Cherian, M. K. Jayaraj, and T. Endo, *Journal of the Ceramic Society of Japan*, **118**, 333 (2010).
27. M. Tortosa, M. Mollar, B. Marí, and F. Lloret, *Journal of Applied Physics*, **104**, 033901 (2008).
28. C.-W. Liu, S.-J. Chang, S. Brahma, C.-H. Hsiao, F. M. Chang, P. H. Wang, and K.-Y. Lo, *Journal of Applied Physics*, **117**, 084315 (2015).
29. W. Zang, P. Li, Y. Fu, L. Xing, and X. Xue, *RSC Adv.*, **5**, 84343 (2015).
30. P. P. Patel, P. J. Hanumantha, O. I. Velikokhatnyi, M. K. Datta, D. Hong, B. Gattu, J. A. Poston, A. Manivannan, and P. N. Kumta, *Journal of Power Sources*, **299**, 11 (2015).
31. M. Willander, O. Nur, J. R. Sadaf, M. I. Qadir, S. Zaman, A. Zainelabdin, N. Bano, and I. Hussain, *Materials*, **3**, 2643 (2010).
32. A. Janotti and C. G. Van de Walle, *Reports on Progress in Physics*, **72**, 126501 (2009).
33. A. B. Djurišić, Y. H. Leung, K. H. Tam, Y. F. Hsu, L. Ding, W. K. Ge, Y. C. Zhong, K. S. Wong, W. K. Chan, H. L. Tam, K. W. Cheah, W. M. Kwok, and D. L. Phillips, *Nanotechnology*, **18**, 095702 (2007).
34. K. H. Tam, C. K. Cheung, Y. H. Leung, A. B. Djurišić, C. C. Ling, C. D. Beling, S. Fung, W. M. Kwok, W. K. Chan, D. L. Phillips, L. Ding, and W. K. Ge, *The Journal of Physical Chemistry B*, **110**, 20865 (2006).
35. C. H. Ahn, Y. Y. Kim, D. C. Kim, S. K. Mohanta, and H. K. Cho, *Journal of Applied Physics*, **105**, 013502 (2009).
36. K. Bandopadhyay and J. Mitra, *RSC Adv.*, **5**, 23540 (2015).
37. D. Li, Y. H. Leung, A. B. Djurišić, Z. T. Liu, M. H. Xie, S. L. Shi, S. J. Xu, and W. K. Chan, *Applied Physics Letters*, **85**, 1601 (2004).
38. J. Kegel, F. Laffir, I. M. Povey, and M. E. Pemble, *Physical chemistry chemical physics: PCCP*, 12255 (2017).
39. S. Chen and L.-W. Wang, *Chemistry of Materials*, **24**, 3659 (2012).
40. A. L. Rudd and C. B. Breslin, *Electrochimica Acta*, **45**, 1571 (2000).
41. S. G. Kumar and K. S. R. K. Rao, *RSC Adv.*, **5**, 3306 (2015).
42. Y. W. Chen, J. D. Prange, S. Duhnen, Y. Park, M. Gunji, C. E. Chidsey, and P. C. McIntyre, *Nature materials*, **10**, 539 (2011).
43. M. R. Shaner, S. Hu, K. Sun, and N. S. Lewis, *Energy & Environmental Science*, **8**, 203 (2015).
44. A. G. Scheuermann and P. C. McIntyre, *J Phys Chem Lett*, **7**, 2867 (2016).
45. F. Kayaci, S. Vempati, I. Donmez, N. Biyikli, and T. Uyar, *Nanoscale*, **6**, 10224 (2014).
46. F. Liu, Y. H. Leung, A. B. Djurišić, A. M. C. Ng, and W. K. Chan, *The Journal of Physical Chemistry C*, **117**, 12218 (2013).
47. J. Al-Sabahi, T. Bora, M. Al-Abri, and J. Dutta, *Materials*, **9**, 238 (2016).
48. A. R. Bielinski, E. Kazyak, C. M. Schlepütz, H. J. Jung, K. N. Wood, and N. P. Dasgupta, *Chemistry of Materials*, **27**, 4799 (2015).
49. A. R. Bielinski, M. Boban, Y. He, E. Kazyak, D. H. Lee, C. Wang, A. Tuteja, and N. P. Dasgupta, *ACS Nano*, **11**, 478 (2017).
50. L. E. Greene, M. Law, J. Goldberger, F. Kim, J. C. Johnson, Y. Zhang, R. J. Saykally, and P. Yang, *Angewandte Chemie*, **42**, 3031 (2003).
51. J. Kegel, J. Halpin, F. Laffir, I. M. Povey, and M. E. Pemble, *CrystEngComm*, **19**, 1938 (2017).
52. L. Yanmei, F. Qingqing, W. Mingzai, L. Yan, L. Qingrong, Z. Jun, and W. Baoming, *Journal of Physics D: Applied Physics*, **40**, 4592 (2007).
53. X. He, H. Yang, Z. Chen, and S. S. Y. Liao, *Physica B: Condensed Matter*, **407**, 2895 (2012).
54. D. A. Schwartz, N. S. Norberg, Q. P. Nguyen, J. M. Parker, and D. R. Gamelin, *Journal of the American Chemical Society*, **125**, 13205 (2003).
55. S. Baruah and J. Dutta, *Science and Technology of Advanced Materials*, **10**, 013001 (2009).
56. R. Xie, T. Sekiguchi, T. Ishigaki, N. Ohashi, D. Li, D. Yang, B. Liu, and Y. Bando, *Applied Physics Letters*, **88**, 134103 (2006).
57. C. G. Van de Walle, *Physica B: Condensed Matter*, **308–310**, 899 (2001).
58. C. H. Patterson, *Physical Review B*, **74** (2006).
59. A. Janotti and C. G. Van de Walle, *Physical Review B*, **76**, 165202 (2007).
60. D.-H. Kim, G.-W. Lee, and Y.-C. Kim, *Solid State Communications*, **152**, 1711 (2012).
61. Y.-S. Kim and C. H. Park, *Physical Review Letters*, **102**, 086403 (2009).
62. L. S. Vlasenko and G. D. Watkins, *Physical Review B*, **71** (2005).
63. P. Cendula, S. D. Tilley, S. Gimenez, J. Bisquert, M. Schmid, M. Grätzel, and J. O. Schumacher, *The Journal of Physical Chemistry C*, **118**, 29599 (2014).
64. Y. K. Gaudy and S. Haussener, *J. Mater. Chem. A*, **4**, 3100 (2016).
65. J. Tauc, *Materials Research Bulletin*, **3**, 37 (1968).
66. M. Liu, C.-Y. Nam, C. T. Black, J. Kamcev, and L. Zhang, *The Journal of Physical Chemistry C*, **117**, 13396 (2013).
67. W. Ma, Z. Lu, and M. Zhang, *Applied Physics A*, **66**, 621 (1998).
68. M. Zukalova, M. Bousa, Z. Bastl, I. Jirka, and L. Kavan, *The Journal of Physical Chemistry C*, **118**, 25970 (2014).
69. D. Liu, Z. Wei, Y. Shen, S. D. Sajjad, Y. Hao, and F. Liu, *J. Mater. Chem. A*, **3**, 20322 (2015).
70. H. Pelouchova, P. Janda, J. Weber, and L. Kavan, *Journal of Electroanalytical Chemistry*, **566**, 73 (2004).
71. J. Kegel, I. M. Povey, and M. E. Pemble, *ECS Transactions*, **77**, 43 (2017).
72. R. L. Doyle and M. E. G. Lyons, 41 (2016).